Journal of Colloid and Interface Science 584 (2021) 647–659

Contents lists available at ScienceDirect

Journal of Colloid and Interface Science

journal homepage: www.elsevier.com/locate/jcis

Regular Article

Diatom-inspired self-assembly for silica thin sheets of perpendicular nanochannels

Yi-Qi Yeh [a,b], Chun-Jen Su [a], Chen-An Wang [a], Ying-Chu Lai [b], Chih-Yuan Tang [c], Zhenyu Di [d], Henrich Frielinghaus [d], An-Chung Su [e], U-Ser Jeng [a,e,*], Chung-Yuan Mou [b,*]

[a] National Synchrotron Radiation Research Center, Hsinchu Science Park, Hsinchu 30076, Taiwan
[b] Department of Chemistry and Center of Condensed Matter Sciences, National Taiwan University, Taipei 10617, Taiwan
[c] Instrumentation Center, National Taiwan University, Taipei 10617, Taiwan
[d] Forschungszentrum Jülich GmbH, Jülich Centre for Neutron Science JCNS, Outstation at MLZ, Garching 85747, Germany
[e] Department of Chemical Engineering, National Tsing Hua University, Hsinchu 30013, Taiwan

GRAPHICAL ABSTRACT

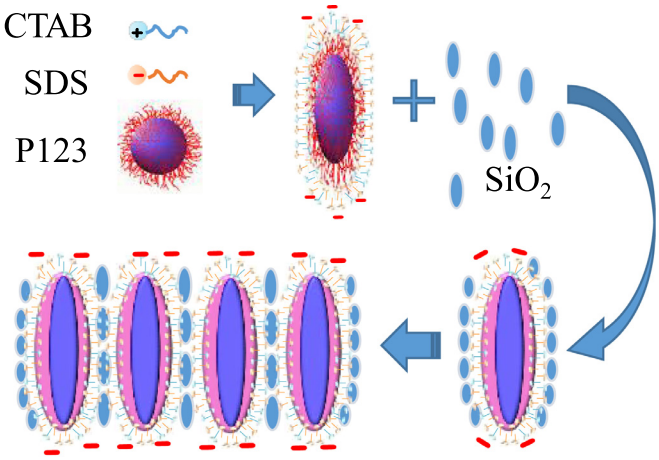

ARTICLE INFO

Article history:
Received 18 July 2020
Revised 25 October 2020
Accepted 26 October 2020
Available online 4 November 2020

Keywords:
Silicate transport micelles
Small-angle X-ray and neutron scattering
Freeze-fracture replica transmission electron microscopy

ABSTRACT

Hypothesis: Multistage silicate self-organization into light-weight, high-strength, hierarchically patterned diatom frustules carries hints for innovative silica-based nanomaterials. With sodium silicate in a biomimetic sol-gel system templated by a tri-surfactant system of hexadecyltrimethylammonium bromide, sodium dodecylsulfate, and poly(oxyethylene-*b*-oxypropylene-*b*-oxyethylene) (P123), mesoporous silica nanochannel plates with perpendicular channel orientation are synthesized. The formation process, analogous to that of diatom frustules, is postulated to be directed by an oriented self-assembly of the block copolymer micelles shelled with charged catanionic surfactants upon silication.
Experiments: The postulated formation process for the oriented silica nanochannel plates was investigated using time-resolved small-angle X-ray and neutron scattering (SAXS/SANS) and freeze fracture replication transmission electron microscopy (FFR-TEM).

* Corresponding authors at: National Synchrotron Radiation Research Center, 101 Hsin-Ann Road, Hsinchu Science Park, Hsinchu 30076, Taiwan (US. Jeng) and Department of Chemistry and Center of Condensed Matter Sciences, National Taiwan University, Taipei 10617, Taiwan (C.Y. Mou).
E-mail addresses: usjeng@nsrrc.org.tw (U-Ser Jeng), cymou@ntu.edu.tw (C.-Y. Mou).

https://doi.org/10.1016/j.jcis.2020.10.114
0021-9797/© 2020 The Author(s). Published by Elsevier Inc.
This is an open access article under the CC BY-NC-ND license (http://creativecommons.org/licenses/by-nc-nd/4.0/).

Silica nanochannels with perpendicular orientation

Findings: With fine-tuned molar ratios of the anionic, cationic, and nonionic surfactants, the catanionic combination and the nonionic copolymer form charged, prolate ternary micelles in aqueous solutions, which further develop into prototype monolayered micellar plates. The prolate shape and maximized surfactant adsorption of the complex micelles, revealed from combined SAXS/SANS analysis, are of critical importance in the subsequent micellar self-assembly upon silicate deposition. Time-resolved SAXS and FFR-TEM indicate that the silicate complex micelles coalesce laterally into the prototype micellar nanoplates, which further fuse with one another into large sheets of monolayered silicate micelles of in-plane lamellar packing. Upon silica polymerization, the in-plane lamellar packing of the micelles further transforms to 2D hexagonal packing of vertically oriented silicate channels. The unveiled structural features and their evolution not only elucidate the previously unresolved self-assembly process of through-thickness silica nanochannels but also open a new line of research mimicking free-standing frustules of diatoms.

© 2020 The Author(s). Published by Elsevier Inc. This is an open access article under the CC BY-NC-ND license (http://creativecommons.org/licenses/by-nc-nd/4.0/).

1. Introduction

Specific biofunctions often rely on astonishing ordering and patterns of associated biostructures [1,2]. Recently, these structure–function correlations inspired an extensive development of biomimetic materials [3,4]. In the case of diatoms, whose silica shells referred as frustules [5–9] are self-organized by their living organic compartments into high-strength, light-weight, and hierarchically patterned (nano- to micro-scaled) architectures, which are of particular interest in search of new silica-based nanomaterials for membrane filtration, biosensors, and drug carriers [2,10,11]. Silica wall structures of diatoms are implemented inside membrane-bound compartments called silica deposition vesicles (SDV) [5]. Within the SDV, specific soluble proteins form complexes with long chain polyamines that can direct the deposition of silica sources and subsequent polymerization into mesoscale-patterned silica walls [5,12]. Such a wall morphogenesis process with SDV for hierarchical frustules also involves sophisticated silica templating with the cytoskeleton and actin filaments of single-cell diatoms [12,13].

Inspired by the biomineralization of diatoms, outstanding development of general methods of creating rich 3D biomimetic silica nanostructures on the basis of DNA origami scaffolds was reported very recently [11]. Via an organic–inorganic self-assembling, we also demonstrated previously [14] a process for forming highly oriented and 2D-ordered silica channel-sheet structures with perpendicular channels of through pores. The corresponding silicate deposition and polymerization were directed by an organic template system comprising of Pluronic triblock (PEO-PPO-PEO) (P123) copolymer micelles deposited with a shell of catanionic surfactant bilayers (of paired cationic and anionic surfactants) [15]; which self-assembly behavior was shown to alter with the mixing ratio of the cationic and anionic surfactants, in addition to acidity and temperature [16,17]. The resultant free-standing silica plates of perpendicular nanochannels were referred to as SBA(⊥) (SBA stands for Santa Barbara Amorphous) [16,17]. Despite the synthesis of SBA(⊥) being of long-term interest and wide applications after its first demonstration [18–22], to date, there is only speculation without direct evidence on how the primary silicate-deposited micelles could evolve into featured monolayered silica nanochannels of perpendicular orientation. The major hurdle lies in the inseparable contributions of the quaternary (copolymer, cationic and anionic surfactants, and silicate source) self-assembly process in solution. A mechanistic understanding of the highly interesting formation process would open a new line of research mimicking the free-standing frustule of diatoms [10–12,23].

Using small-angle X-ray and neutron scattering (SAXS and SANS), grazing-incidence SAXS (GISAXS), and freeze-fracture replication transmission electron microscopy (FFR-TEM), we could unveil the critical micellar structures and their self-assembly process that govern the formation of SBA(⊥). Specifically, controlled condensation of charged catanionic surfactant bilayers on neat spherical P123 micelles is found to significantly elongate the micelles into negatively charged prolate ones of an optimized aspect ratio ca. 3.0. The charge and shape of the complex micelles together play a pivotal role in directing a lateral self-assembly of the micelles upon silicate condensation, resulting in large sheet-like silicate aggregates of in-plane lamellar ordering. Further ordered structural transition driven by silicate polymerization within the thin aggregate plates redistributes the deposited silicate source into 2D-hexagonally packed cylinder nanochannels, of uniform channel length and perpendicular orientation to the plate. Depending on environmental controls, these silica channel plates can selectively coalescence laterally further for enlarged 2D ordered sheets or stack vertically for Moiré patterns of 3D organized structures [17]. In this study, we show that adsorption of catanionic surfactants can modify the shape and charge of the template P123 micelles for acting as silica transport micelles (ca. 15 nm), whose nanoplate aggregates (ca. 150–200 nm) further serve as seeds of silica deposition platforms, mimicking frustule formation of diatoms. We note that, despite abundant studies on binary micelles of P123 adsorbed with anionic- or cationic-surfactants, SAXS or SANS on ternary micelles of pluronic copolymers, SDS, and cationic surfactants, is seldom reported up to date.

2. Materials and methods

2.1. Sample preparation

Hexadecyltrimethylammonium bromide (C_{16}TAB, 99+%, Acros Organics), sodium dodecylsulfate (SDS, 99%, Acros Organics), and poly(oxyethylene-*b*-oxypropylene-*b*-oxyethylene) ($EO_{20}PO_{70}EO_{20}$, P123) of an average molecular mass 5800 Da (Sigma-Aldrich, reported polydispersity index ~ 1.1), were used in sample preparation for ternary mixtures of different molar ratios of R = [SDS]/[C_{16}TAB] from 1.3 to 2.0 and x = [SDS]/[P123] from 0 to 52. The sample solution of an optimum yield of SBA(⊥) comprised 20.6 mM SDS, 13.7 mM C_{16}TAB, and 0.8 mM P123, corresponding to R = 1.5 and x = 26. Sodium silicate (27 wt% SiO_2, 4 wt% NaOH, and 69 wt% H_2O) of 80 mM was further added into the surfactant-P123 sample solution under stir for a few hours at 318 K, with pH values between 4 and 5 adjusted by sulfuric acid and sodium hydroxide. Within this pH-range, similar silica channels of same packing features of SBA(⊥) could be formed [16]. Deuterated SDS (d-SDS, 98 atom % D, CDN Isotopes) and deuterated C_{16}TAB (d-C_{16}TAB, 98 atom % D, CDN Isotopes), and D_2O (99.8 atom % D, Acros Organics) were used in preparation of SANS sample solutions.

2.2. TEM and freeze-fracture replication TEM

Freeze-fracture replication TEM was performed with a Balzers freeze-fracture apparatus (BAF 400 D). The liquid sample was dropped in between two electron-microscopic gold sandwich holders, then plunged altogether into nitrogen slush (a mixture of liquid and solid forms of nitrogen at 63 K for a faster sample cooling rate, compared to liquid nitrogen alone at 77 K). Subsequently, the sample was submerged into a liquid nitrogen reservoir and transferred into a sample-fracture housing precooled in liquid nitrogen. The frozen sample was further inserted into a vacuum chamber maintained at 168 K for split open into fractures. The fracture surfaces were first shadowed (at an angle of 30°) with a 2-nm layer of platinum–carbon, followed by coating with a 20-nm carbon layer (at 90°). The replicas retrieved from the thawed samples were cleaned in deionized water, then mounted on copper grids for TEM observation (Hitachi S-7100, 75 keV) at room temperature.

2.3. Small angle scattering (SAS)

2.3.1. SAS model

The SANS and SAXS intensity profiles of the colloidal solutions of P123 and the catanionic surfactants were modeled as

$$I(q) = I_L P_L(q) S_L(q) + I_o P(q) S(q) + I_{inc} \quad (1)$$

where I_L and I_o are the zero-angle (q = 0) scattering intensities for coexisting large aggregates and small micelles, of respectively normalized form factors $P_L(q)$ and $P(q)$, with $P(0)$ = 1 [24]. In Eq. (1), $S_L(q)$ and $S(q)$ are the corresponding structure factors; I_{inc} is the constant incoherent scattering background, which is much more pronounced in SANS than that in SAXS [24]. For core–shell micelles of an ellipsoidal shape

$$P(q) = \int_0^1 \left[\frac{W_c - W_s \frac{V_c}{V_s}}{W_c + W_s} 3j_1(u_c)/u_c + \frac{W_s + W_s \frac{V_c}{V_s}}{W_c + W_s} 3j_1(u_s)/u_s \right]^2 d\upsilon \quad (2)$$

where $u_c = q[a_c^2\upsilon^2 + b_c^2(1-\upsilon^2)]^{1/2}$, $u_s = q[a^2\upsilon^2 + b^2(1-\upsilon^2)]^{1/2}$, with the orientation factor υ of the ellipsoid; $j_1(X) = (\sin X - X\cos X)/X^2$ is the spherical Bessel function of the first order [24] with $3j_1(X)/X$ = 1 at X = 0 (i.e. q = 0). The parameters a_c and b_c are for the semi-major and semi-minor axes of the ellipsoidal core, and a and b are that of the overall core–shell ellipsoid (Fig. 1) [24,25]; $W_c = (\rho_c - \rho_w)V_c$ and $W_s = (\rho_s - \rho_w)V_s$ are volume-weighted scattering contrasts of the core ρ_c and the shell ρ_s with respect to the water solvent ρ_w, with the core volume $V_c = (4/3)\pi a_c b_c^2$ and shell volume $V_s = (4/3)\pi(ab^2 - a_c b_c^2)$ [25]. The aspect ratio of a prolate spheroid is defined by $\delta = a/b$, which reduces to 1 for spheres ($a = b$). The size polydispersity in the core–shell form factor (Eq. (2)) was taken into account using the Schulz function [26] as expressed in Eq. S-1 and S-2, in the Supporting Information (SI).

With SANS, we selectively used deuterated surfactants (mainly deuterated aliphatic chains) with neutron scattering-length-densities (SLD) matching closely to that of D_2O; such a contrast selection allowed better clarification of the scattering contribution of P123 micelles from that of surfactants in the complex surfactant-P123 micelles in D_2O solution [27–29]. By contrast, SAXS is sensitive to the core–shell structures of the overall P123-surfactant complex micelles owing to the higher X-ray SLD values of the EO block of P123 and the headgroups of the catanionic surfactants, compared to that of the PO core and aqueous solution [27], as illustrated in Fig. 1 and Fig. S-1. Interparticle interference effect on the SANS/SAXS profiles of the charged complex micelles of P123 and surfactants was taken into account by a structure factor obtained with the rescaled mean spherical approximation (MSA) $S(q)_{MSA}$ [30,31], assuming rigid charged spheres interacting through a screened Coulomb potential of an effective hard-sphere diameter σ.

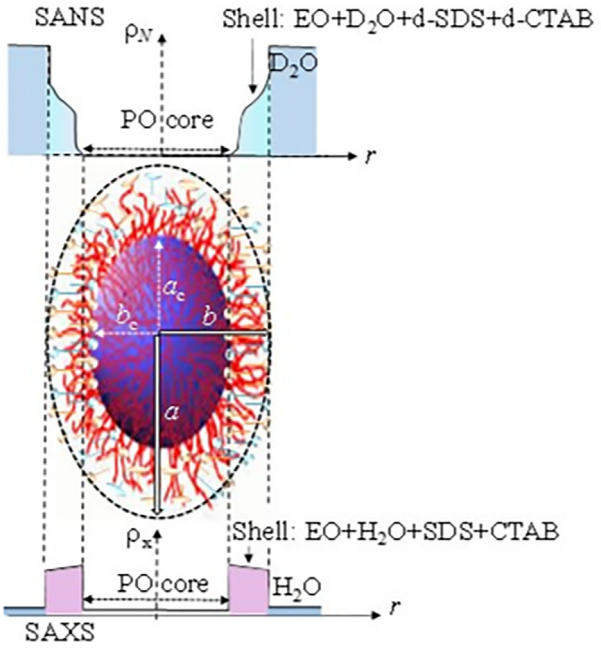

Fig. 1. Neutron and X-ray SLD profiles, ρ_N (top) and ρ_x (bottom), for a simplified core–shell ellipsoidal model of P123 micelles deposited with aliphatic-chain deuterated SDS (d-SDS) and C_{16}TAB (d-C_{16}TAB) in D_2O for SANS, and with non-deuterated SDS and C_{16}TAB in H_2O for SAXS. a_c and b_c are the semi-major and semi-minor axes of the PO-core (colored in blue) of the P123 micelle, whereas a and b are that of the overall prolate micelle, including the hydrated EO shell (red) intercalated with the catanionic surfactants. The PO and EO groups are of ρ_N values of 0.343 and 0.638 and ρ_x values of 9.24 and 10.4, in units of 10^{-6} Å^{-2} [27]. Note that the core size is contributed mainly by the PO region of low SLD, with the PO-EO interface broadened more in SANS due to a similarly low ρ_N value of the EO group. Note that the EO zone away from the interface is of increasingly higher ρ_N due to hydration with D_2O of relatively high ρ_N = 6.39 × 10^{-6} Å^{-2} (at 20 °C). This smearing effect is less evident in SAXS, owing to the relatively high ρ_x of the EO group, with respective to the PO group and H_2O of ρ_x = 9.47 × 10^{-6} Å^{-2}. (For interpretation of the references to colour in this figure legend, the reader is referred to the web version of this article.)

The forward scattering intensity I_o (at q = 0) of the ternary micelles depends on the SDS and C_{16}TAB adsorption numbers, N_s and N_{ct}, and the aggregation number N_p of P123:

$$I_o = n[N_p \Delta\rho_p V_p + N_s \Delta\rho_s V_s + N_{ct} \Delta\rho_{ct} V_{ct}]^2 \quad (3)$$

with scattering contrasts (difference in the SLD with respect to that of solvent ρ_w) $\Delta\rho_p = \rho_p - \rho_w$, $\Delta\rho_s = \rho_s - \rho_w$, and $\Delta\rho_{ct} = \rho_{ct} - \rho_w$, and the partial specific volumes V_p, V_s, and V_{ct}, of P123, SDS, and C_{16}TAB, respectively [25,26,32]. Here, the number density of the P123 micelles in solution, $n = (C_p - C_L - C_{p\text{-CMC}})/N_p$ is defined by the total copolymer concentrations C_p in solution and C_L in the large aggregates, and the critical micelle concentration $C_{p\text{-CMC}}$ [29]. $C_{p\text{-CMC}}$ of P123 in solutions with SDS was reported to be 0.043 mM [33], which is negligibly small compared to that (0.8 mM) used in this study. In principle, the three parameters N_p, N_s, and N_{ct} of the micelle composition could be deduced model-independently, using three different values of X-ray $I_{o,X}$ and/or neutron $I_{o,N}$ (in the absolute scattering intensity scales of units of cm^{-1}) of Eq. (3) via contrast variations. In our case, anionic SDS and cationic C_{16}TAB could form ion pairs and self-assemble into mixed bilayers due to strong charge interactions [15,34–37]. Moreover, the critical aggregation concentrations of SDS and CTAB in their mixtures were shown to be below 0.5 mM [15,36], which is substantially smaller than the catanionic surfactant concentrations

used in our sample solutions (above 10 mM). Therefore, most of SDS and C_{16}TAB surfactants were expected to co-condense on P123 micelles. Namely, the adsorption ratio of SDS/C_{16}TAB would be close to that of the total catanionic surfactants in solution [15], i.e. $N_s/N_{ct} \cong R$. With the approximation of $N_{ct} = N_s/R$, we could deduce N_p and N_s with only two I_0 values of Eq. (3) from SANS and SAXS, as shown below:

$$N_p = (I_{o,X}/n)^{1/2}/(A_X + \chi_s B_X) \quad (4)$$

$$N_s = \chi_s N_p \quad (5)$$

$$\text{with } \chi_s = (\mu A_N - A_X)/(\mu B_N - B_X) \quad (6)$$

Here, $A_X = V_p\Delta\rho_{p\text{-}X}$, $A_N = V_p\Delta\rho_{p\text{-}N}$, $B_X = V_s\Delta\rho_{s\text{-}X} + (V_{ct}/R)\Delta\rho_{ct\text{-}X}$, $B_N = V_s\Delta\rho_{s\text{-}N} + (V_{ct}/R)\Delta\rho_{ct\text{-}N}$, and the square root of the X-ray/neutron zero-angle scattering intensity ratio $\mu = \pm(I_{o,X}/I_{o,N})^{1/2}$. For the ternary micelles with limited size polydispersity, N_p, N_s, and N_{ct} in Eqs. (4) and (5) would correspond to mean values, when derived from the corresponding mean I_o values. In the above consideration, we have neglected the unlikely occurred cases of surfactant-segregated SDS/P123 and C_{16}TAB/P123 binary micelles in the ternary mixture; they are simply energetically not favored due to the strong charge pair interactions of the catanionic surfactants, as indicated in previous reports [33–37].

The level of heterogeneity (or degree of phase segregation) of the ternary mixture is quantified by the scattering invariant [24]

$$Q \equiv \int_0^\infty I(q)q^2dq. \quad (7)$$

For convenience, a relative scattering invariant can be calculated with the upper and lower limits of the integration approximated by the high-q and low-q limits of an interested q-range that can cover the major changes in structural features of the complex micelles.

2.3.2. SAS measurements

SAXS measurements were performed at the 23A SWAXS beamline of the Taiwan Light Source of the National Synchrotron Radiation Research Center in Hsinchu [38]. With a beam of 12.0 keV (X-ray wavelength λ = 1.033 Å filtered with a double-multilayer monochromator for 1% dispersion in λ) and a sample-to-detector distance of 3048 mm, SAXS data were collected at 318 K sample temperature using an area detector MARCCD165. The scattering vector $q = 4\pi\lambda^{-1}\sin\theta$, defined by the scattering angle 2θ and λ, was calibrated with a silver behenate standard. The SAXS data collected were corrected for transmission (measured directly using the MARCCD165 with an attenuated direct beam), background, and pixel sensitivity of the detector; the 2D SAXS patterns were circularly averaged into 1D intensity distribution function $I(q)$, and scaled to the absolute intensity via comparing to the scattering intensity of water [38]. For time-resolved SAXS, sampled solutions were taken out every 5 min. from a composition-optimized solution with silicate source added for in situ reaction under stirring at 318 K. Each loading of the sampled solution to the SAXS cell was within 2 min, which was followed by 10 s of SAXS data collection without sample stirring. The SAXS cell was sealed with two thin Kapton windows (each of 12 μm thickness) for a 2-mm X-ray path length, and thermostated at a same reaction temperature of 318 K.

Sample solutions parallel to that used in SAXS, but with SDS and C_{16}TAB replaced respectively by aliphatic-chain deuterated SDS and C_{16}TAB, were prepared for SANS measurements. They were carried out at 318 K sample temperature at the FRM II research reactor in Garching, Germany, using the small-angle scattering diffractometer at the KWS-1 beamline [39]. With a neutron wavelength of 4.5 Å and three sample-detector distances of 1.7, 7.7, and 19.7 m (with corresponding collimation distances of 2, 8, and 20 m), the data covered a wide q-range of 0.003 – 0.3 $Å^{-1}$. All transmissions were measured simultaneously with SANS data collections using a monitor embedded inside the beamstop. The SANS data were corrected in terms of detector efficiency and parallax, calibrated with the transmission, sample thickness, and detector pixel solid angle, and placed in the absolute scattering intensity via the scattering of a 1.5-mm thick Plexiglas sample as a secondary reference standard. The SANS instrumental q-resolution (shown in Fig. S-2, SI), was included in the model fitting of the data using the SasView (version 4.2.2) analysis package (http://www.sasview.org/).

3. Results and discussion

3.1. Imaging results

We first examined the self-assembly of the ternary system of SDS, C_{16}TAB, and P123 for the shape changes of P123 micelles induced by condensation of the catanionic surfactants. Shown in Fig. 2 are a series of FFR-TEM images of the complex micelles of P123 condensed with the catanionic surfactants of mixing ratios R ranging from 1.2 to 2.0 (keeping a constant C_{16}TAB concentration of 13.9 mM). When R is higher than 1.8 (substantially excess SDS), the copolymer micelles deposited with significantly negatively charged catanionic surfactants are largely dispersed without much aggregation as revealed in Fig. 2a,b. Upon silicate addition, these micelles aggregated with no directional preference, resulting in clustered silicate particulates (Fig. 3a,b). When R = 1.5 – 1.67, a substantial amount of dispersed P123-surfactant micelles (~15 nm in size) were observed. Also observed in the same images are relatively large nanoplate aggregates with lateral dimensions of ca. 150–200 nm and a thickness (~15 nm) of ca. the size of the complex micelle (Fig. 2c,d), suggesting that these nanoplates are largely monolayers of the complex micelles. Upon silicate deposition, the small dispersed silicate micelles coalesced to the seeded nanoplates (nuclei of self-assembly), and developed into large and thin silicate sheets. These silicate sheets maintained the planar conformation during calcining (as evidenced in Fig. 3c,d) for vertically oriented silica channels within (as shown below). With R reduced to 1.3–1.2 for relatively charge-neutralized catanionic surfactants, the resultant P123-surfactant micelles form dominantly large plate aggregates (Fig. 2e,f), leaving only sparsely dispersed micelles. After silicate deposition and calcination, these large sheets, however, fractured into small pieces as shown in Fig. 3e,f.

These FFR-TEM results reveal the critical importance of coexistence of the two kinds of surfactant-P123 self-assemblies in particularly Fig. 2d—the charged micelles named as silica transport micelles (STM) and the nanoplate aggregates of monolayered micelles named as silica deposition nanoplates (SDNP). The terms STM and SDNP are inspired by the frustule formation process in diatoms mentioned previously. The close analog of our system with biomineralization in diatoms is discussed further below. For now, we simply use STM and SDNP for those observed in Fig. 2.

3.2. Scattering results

3.2.1. P123 micellar structures modified by catanionic surfactants

Shown in Fig. 4a are the SANS data for the sample solutions of a wide range of x (=[SDS]/[P123]), ranging from 0 to 52 (keeping R = 1.5 and constant 0.8 mM P123). All the SANS data can be fitted on the basis of the core–shell ellipsoidal model detailed previously. Specifically, the data for the case of neat P123 micelles could be fitted using the spherical core–shell model (i.e. $a = b$ and $a_c = b_c$), with

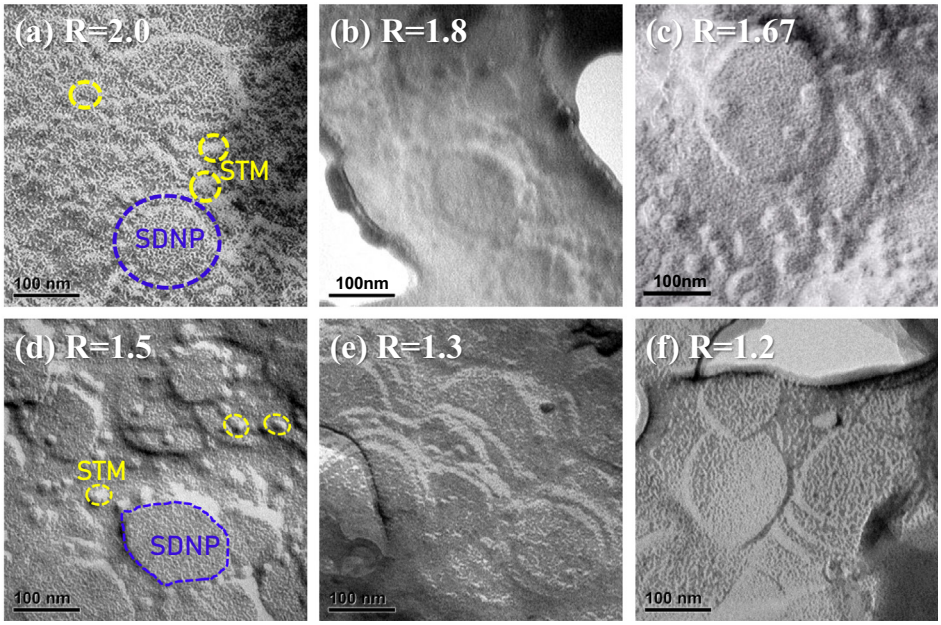

Fig. 2. FFR-TEM images for the complex micelles and plate aggregates of P123 and the catanionic surfactants of SDS and C_{16}TAB, with surfactant mixing ratio *R* ranging from 2.0 to 1.2. Samples were prepared in solutions of pH = 5.0 at 318 K. Circled in (a) and (d) are the large aggregate plates named silica deposition nanoplates (SDNP) and the small silica transportation micelles (STM); which two are comparably populated in the case *R* = 1.5 in (d). All scale bars represent 100 nm.

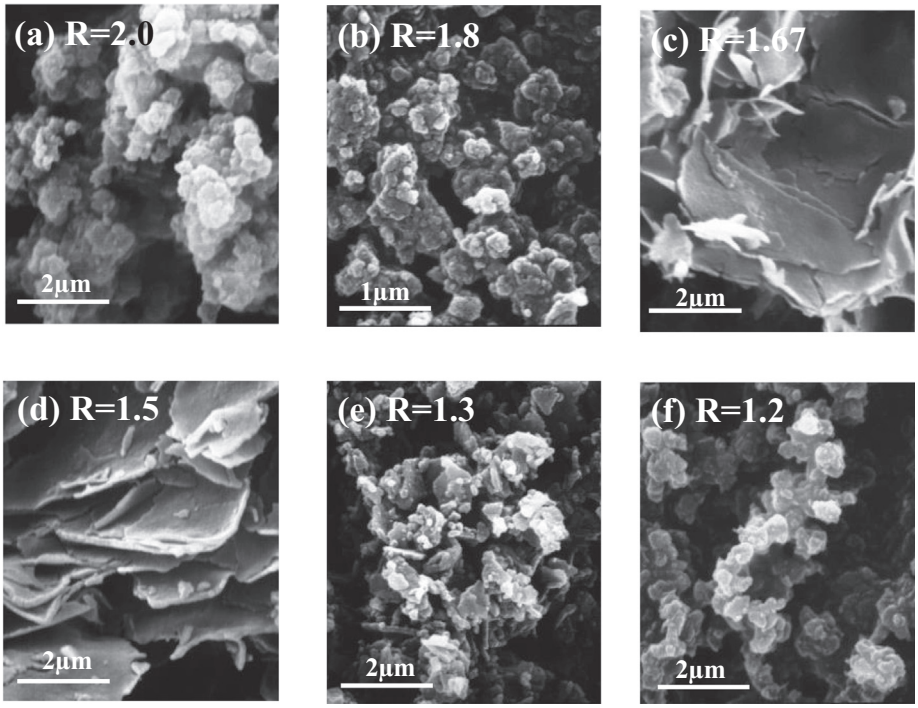

Fig. 3. SEM images of the calcined samples corresponding to those shown in Fig. 2.

a size polydispersity *p* of ~15% (cf. Table S-1). The fitted parameters summarized in Table 1 are consistent with those reported previously [27]. With x = 0.5, the SANS data were fitted with core–shell spheres, together with a rescaled MSA structure factor $S(q)_{MSA}$ [30] to account for the effect of interparticle interactions in the low-q region. With intermediate increase (x < 10) of the surfactant concentration in the P123 solution, the SANS data in the q-range above 0.01 Å^{-1} can still be fitted using the same model of core–shell spheres together with $S(q)_{MSA}$ (Fig. 4a). However, the upturn of the SANS data in the very low-q region below 0.01 Å^{-1} is empirically accounted for (Fig. 4a) using additional scattering contributions of large core–shell spheroids (hundreds of Å) with a hard-sphere structure factor $S(q)_{HS}$, as detailed in Table S-1, SI. With x increased over 10, the corresponding SANS data in the q-region > 0.01 Å^{-1} could only be fitted reasonably well using prolate core–shell spheroids together with $S(q)_{MSA}$, indicating that significant adsorption of the catanionic surfactants to the P123 micelles could lead to micellar shape transition (cf. Table 1). All the fitted

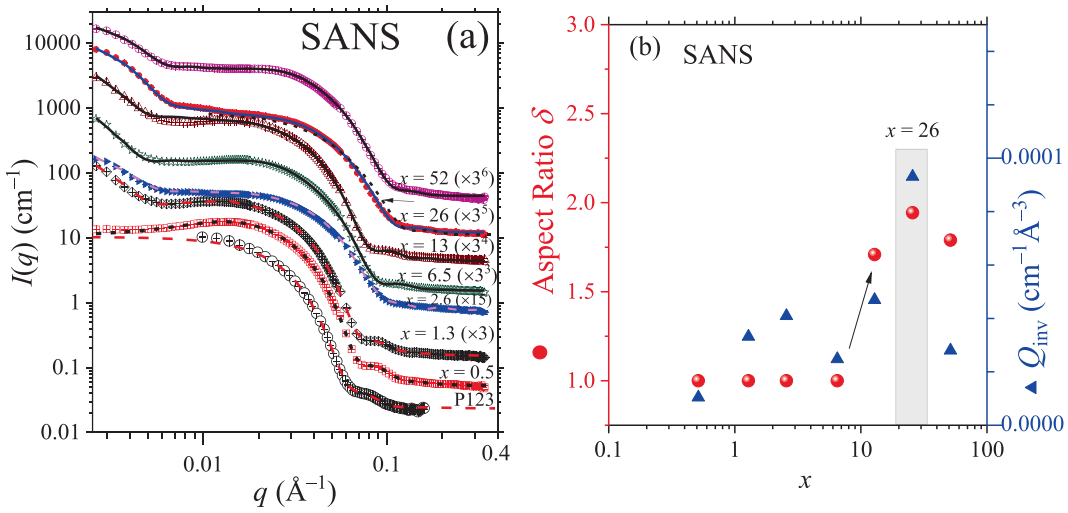

Fig. 4. (a) SANS profiles of the D_2O solutions of deuterated-SDS, deuterated-C_{16}TAB, and P123, with varied x = [SDS]/[P123], at fixed R = 1.5 and [P123] = 0.8 mM. The profiles are scaled up from the absolute intensity by the factors indicated in the brackets. These profiles are fitted (solid curves) respectively using core–shell spheres for the cases with x < 10 and core–shell prolate spheroids with x > 10, with $S(q)_{MSA}$ incorporated in all cases (expect the case of neat P123). The upturn data in the very low q-region are described by scattering from additional large aggregates. All the fitted parameters are summarized in Table S-1. Note that the small data error bars are largely within the data symbols. The core–shell sphere model could not describe well the representative data with x = 26, as shown with the hence fitted (dotted) curve (indicated by an arrow). (b) Corresponding mean aspect ratio δ defined by $\bar{a}/\bar{b}$ and Q_{inv} deduced from the fitted parameters, which are concomitantly maximized at x = 26 (the shaded zone). The arrow near x = 10 marks a sphere-to-ellipsoid shape transition of the micelles.

Table 1
Fitted size parameters of the small core–shell micelles using the SANS profiles in Fig. 4a. The data with x = 13, 26, or 52 are fitted with a model of core–shell prolate spheroids, with mean semi-major and semi-minor core axes $\bar{a}_c$ and $\bar{b}_c$ and corresponding $\bar{a}$ and $\bar{b}$ for the overall prolate shape. Data with $x \leq 6.5$ are fitted with core–shell spheres of $\bar{a}_c = \bar{b}_c$ and $\bar{a}$ and $\bar{b}$. Complete fitting parameters are detailed in Table S-1.

	x = [SDS]/[P123]	$\bar{a}_c$ (Å)	$\bar{b}_c$ (Å)	$\bar{a}$(Å)	$\bar{b}$(Å)
Core-Shell Sphere	0	63.2 ± 0.2		89.2 ± 0.5	
$\bar{a}_c = \bar{b}_c$	0.5	58.6 ± 0.1		89.1 ± 0.1	
	1.3	56.8 ± 0.1		84.1 ± 0.1	
	2.6	29.1 ± 0.1		62.2 ± 0.1	
	6.5	44.7 ± 0.1		64.7 ± 0.1	
Core-Shell Ellipsoid	13	50.1 ± 0.9	20.5 ± 0.2	88.5 ± 1.2	51.8 ± 0.2
	26	64.4 ± 14.4	26.3 ± 3.6	78.7 ± 8.7	40.5 ± 3.6
	52	68.4 ± 0.6	28.5 ± 0.1	74.2 ± 1.3	43.0 ± 0.1

structural parameters of the small micelles and the aggregates are summarized in Table S-1; the key structure parameters in Table 1 reveal that the sizes of the micelles decrease systematically with increase of the surfactant concentration.

Previously, Mansour *et al.* [29] also found with SANS that spherical core–shell P123 micelles could be deformed into ellipsoidal ones when adsorption of SDS to P123 micelles was>30% volume fraction of the binary micelles [29]. Here, the ternary micelles of SDS/C_{16}TAB/P123 elongate for a prolate shape gradually with x increased over 10, as indicated by the increased δ values shown in Fig. 4b. At x = 26 (and R = 1.5), corresponding to a solution composition of optimized yield of the final SBA(⊥) product [16], not only δ but also the scattering invariant Q_{inv} (degree of nano-phase segregation) are maximized; which two values start decaying after x > 26.

We further tuned the SDS/C_{16}TAB ratio (within R = 1.3 – 2.0) in the solutions of P123 and the catanionic surfactants (keeping a constant C_{16}TAB concentration). The corresponding SANS profiles (Fig. 5a) reveal successive size changes of the complex micelles. Specifically, the shoulder position of the intensity profile around q = 0.03 Å^{-1} for the case with R = 1.3 shifts gradually to higher q as R increases, corresponding to systematically reduced micellar sizes. In the very low-q region (<0.01 Å^{-1}), the upturn intensity is described by additional scattering contribution from large aggregates, as revealed in the FFR-TEM results (Fig. 2). The low-q scattering intensity is reduced as R increases, suggesting less aggregates of the surfactant-P123 micelles up on increase of SDS. We could fit decently all the SANS data (Fig. 5a) using combined small core–shell prolate spheroids (for the ternary micelles) with $S(q)_{MSA}$ and large core–shell spheroids with $S(q)_{HS}$ [27,31], as that done previously. The fitted parameters are representatively summarized in Table 2 and detailed in Table S-2, SI.

We also conducted parallel SAXS measurements. For consistency, we kept the PO-core density and the parameters used in $S(q)_{MSA}$ of the prolate micelles the same in the parallel SANS and SAXS data fitting processes (cf. Table S-2 and -3, SI). As shown in Fig. 5b, most of the SAXS data are fitted decently using the same model of coexisting core–shell prolate spheroids with $S(q)_{MSA}$ and large core–shell spheroids with $S(q)_{HS}$, as that done in the SANS data fitting. The low-q SAXS data for the cases of R = 1.8 and 2.0 of higher surfactant concentrations, however, could only be qualitatively fitted, due likely to increasingly more surfactant contents of additional scattering contributions that could not be described by the current model. The size parameters fitted for the small prolate micelles are summarized in Table 2. We note that the fitted core sizes of the prolate core–shell micelles from the SANS data tend to be larger than that obtained from the SAXS data fitting. This inconsistency is attributed to the simplified core–shell

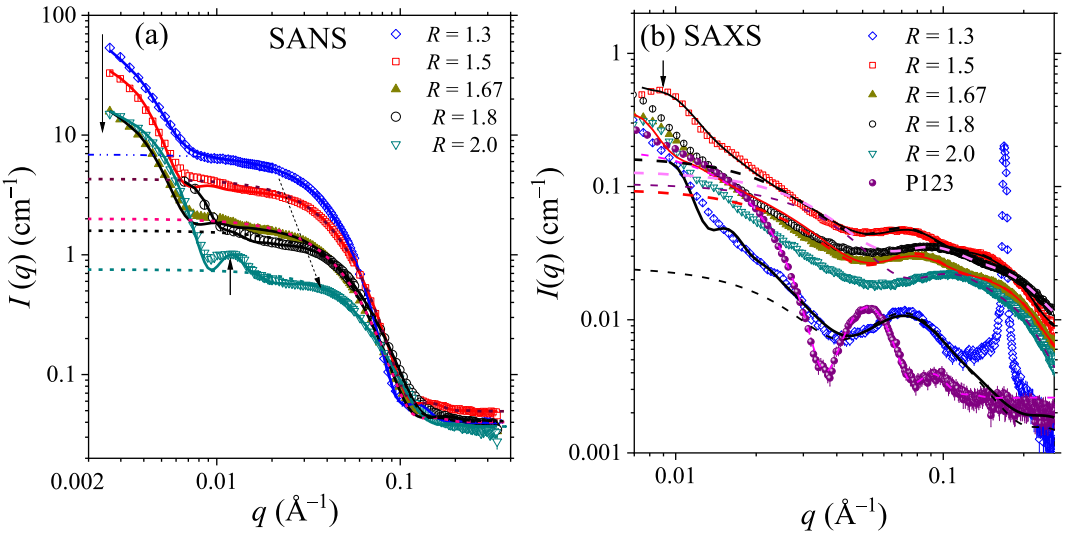

Fig. 5. (a) SANS profiles measured for the D_2O solutions of P123 and deuterated SDS/C_{16}TAB of different surfactant mixing ratios R, with fixed 13.9 mM C_{16}TAB and 10.8 mM P123. Data are fitted (solid curves) using combined large core–shell spheroids with $S(q)_{HS}$ and small core–shell prolate spheroids with $S(q)_{MSA}$. The dotted curves are simulated profiles using solely the fitted form factors of the core–shell prolate spheroid, with the $S(q)_{MSA}$ contribution excluded. The feature humps (selectively indicated by the thick arrows) near q = 0.01 Å^{-1} of the SANS and SXAS profiles are largely contributed by the form factors of large core–shell spheroids. (b) Corresponding SAXS profiles and the data fitting (solid curves). Dashed curves are solely the fitted form factors of the prolate core–shell spheroids. For the case R = 1.3, the sharp peak centered at q = 0.169 Å^{-1} corresponds to a bilayer stacking of the catanionic surfactants. Also shown are the SAXS data of neat P123 micelles, fitted with core–shell spheres (dotted curve).

Table 2
Fitted size parameters of the prolate micelles using the SANS and SAXS data shown in Fig. 5. The mean semi-major and semi-minor axes of the core–shell prolate spheroid model are $\bar{a}_c$ and b_c for the core and $\bar{a}$ and b for the whole prolate shape. The mean aspect ratio δ is defined by $\bar{a}/b$. Those for neat P123 micelles (null R) are also shown for comparison. $I_{o\text{-}x}$ and $I_{o\text{-}N}$ are respectively the zero-angle scattering intensities of SAXS and SANS calculated respectively using the fitted mean form factors of the ternary micelles. The number of hydration water molecules per EO unit of P123 in the prolate micelles, $N_{w\text{-}EO}$, is roughly estimated on the basis of the deduced shell volume of the micelles (from the fitted core–shell dimensions) and the volumes (at 318 K) of water molecule of 30.6 Å^3, EO group of 63.9 Å^3 [27], PO group of 96.0 Å^3 [27], d-SDS of 427 Å^3 [40], and d-C_{16}TAB of 606 Å^3 [41], together with the extracted aggregation number of P123 and adsorption numbers of SDS and C_{16}TAB shown in Fig. 6a,b.

SANS

R	$\bar{a}_c$ (Å)	$\bar{b}_c$ (Å)	$\bar{a}$(Å)	$\bar{b}$(Å)	$I_{o\text{-}N}$(cm^{-1})
Null	63.2 ± 2.0	63.2 ± 2.0	89.2 ± 2.0	89.2 ± 2.0	9.50 ± 0.95
1.3	65.1 ± 1.6	31.9 ± 1.4	79.2 ± 1.0	46.0 ± 1.6	6.87 ± 0.91
1.5	64.4 ± 14.4	26.3 ± 3.6	78.7 ± 8.7	40.5 ± 3.6	4.30 ± 0.55
1.67	54.7 ± 0.1	22.0 ± 0.1	72.5 ± 0.1	39.8 ± 0.1	2.00 ± 0.32
1.8	57.4 ± 15.2	25.3 ± 1.8	62.7 ± 5.4	30.5 ± 1.0	1.59 ± 0.32
2.0	47.6 ± 0.1	21.4 ± 0.1	55.5 ± 0.1	29.4 ± 0.1	0.754 ± 0.12

SAXS

R	$\bar{a}_c$ (Å)	$\bar{b}_c$ (Å)	$\bar{a}$(Å)	$\bar{b}$(Å)	$I_{o\text{-}X}$(cm^{-1})	δ	$N_{w\text{-}EO}$
Null	60.4 ± 0.1	60.4 ± 0.1	96.9 ± 0.2	96.9 ± 0.2	0.202 ± 0.019	1.0	15
1.3	41.9 ± 0.3	25.2 ± 0.1	82.0 ± 0.3	30.7 ± 0.1	0.0250 ± 0.0033	2.68 ± 0.02	22
1.5	50.8 ± 0.1	18.4 ± 0.1	76.0 ± 0.1	24.3 ± 0.1	0.167 ± 0.023	3.13 ± 0.01	8
1.67	45.9 ± 0.8	17.2 ± 0.1	70.8 ± 0.8	22.7 ± 0.1	0.096 ± 0.015	3.12 ± 0.01	9
1.8	36.8 ± 0.1	17.1 ± 0.1	61.7 ± 0.1	23.1 ± 0.1	0.139 ± 0.022	2.67 ± 0.02	*
2.0	26.7 ± 0.4	15.4 ± 0.4	60.3 ± 0.1	23.1 ± 0.2	0.091 ± 0.014	2.61 ± 0.01	23

*Insensitive.

model used, which does not account for the interfacial transition (layer) between the PO-core and the hydrated PEO shell. Affected by a gradient hydration of PEO shell (namely, less hydration toward the core–shell interface), the scattering contrast of the interfacial layer would contribute differently in SAXS and SANS. Specifically, the neutron SLD values of the PO and EO groups of P123 are both much smaller than that of D_2O. Therefore, the PPO-core size of low neutron SLD smears easily with the PPO-PEO interfacial zone, of also low neutron SLD due to lower D_2O hydration at the interface (cf. Fig. 1); this leads to the larger SANS core sizes. By contrast, X-ray SLD of the PEO is significantly higher than that of the PPO and water, Therefore, the PPO core size could be better differentiated by the sharper SLD transition at the core–shell interface in SAXS. Overall, the SANS and SAXS data fitting results provide consistent trends of changes in the micellar shape and overall size.

We also notice a sharp SAXS peak emerged at q = 0.169 Å^{-1} (Fig. 5b) in the case of R = 1.3; the corresponding periodic spacing 3.7 nm extracted from the peak position is consistent with the bilayer spacing observed previously for multilamellar vesicles of SDS and C_{16}TAB [37]. The result reveals formation of stacked catanionic surfactant bilayers when R is reduced to 1.3 towards charge neutralization (i.e. R = 1.0). This bilayer stacking, however, is invisible in the corresponding SANS data, due to low scattering contrast between the deuterated surfactants and D_2O. Similarly, the feature humps in the very low-q regions of the SANS and SXAS profiles (Fig. 5) could be described using form factors of similarly large core–shell spheroids; however, thicker shells are needed for decent

SAXS low-q data fitting (cf. Table S-3, SI), presumably due to enriched surfactant contents (invisible to SANS) in the outer shell zones of the large core–shell spheroids.

Using solely the fitted form factors of the ternary micelles (i.e. excluding the contributions of the structure factor and large aggregates), we calculated the zero-angle intensities of $I_{o\text{-}N}$ and $I_{o\text{-}N}$ of the core–shell prolate micelles (shown in Table 2) to determine the SDS-P123 binding ratio χ_s (=N_s/N_p) using Eq. (6). We, however, could not determine the corresponding N_p and N_s values of the complex micelles from Eq. (4) and (5), as the number density of the complex micelles could not be deduced alone from the total P123 concentration in the solution. This is because of an unknown population of the coexisting large aggregates. Alternatively, we estimated the N_p values using the micellar PPO-core sizes deduced from the SAXS-fitted core parameters and a reported volume of the PO group (96 Å^3) of P123 [26]. With the hence resolved N_p and χ_s values, N_s and N_{ct} could be deduced accordingly, as shown in Fig. 6. We note that the uncertainties of these deduced compositional parameters are not small due to the few approximations used, including $N_{ct} = N_s/R$ based on charge pair co-condensation, N_p from volume conservation, and mean $I_{o\text{-}N}$ and $I_{o\text{-}N}$ values back-calculated from the mean form factors fitted.

The evolution trends of the micellar structure and composition in Fig. 6 reveal critical self-assembly features of the ternary micelles. Specifically, we found that increasing R (via increase of the SDS concentration) could disperse increasingly better P123 micelles for systematically decreased aggregation numbers from N_p = 16 at R = 1.3 to N_p = 4 at R = 2.0 (Fig. 6b); correspondingly, SDS-adsorption affinity increases by more than four folds, from χ_s = 17.6 to 70.5 (Fig. 6a). The enhanced adsorption affinity of the catanionic surfactants with P123 micelles is consistent with that reported previously for binary micelles of SDS/P123 [29]. Facilitated by the charge pair co-condensation, C_{16}TAB-adsorption affinity is enhanced with χ_s by ca. three folds, from $\chi_{ct} = N_{ct}/N_p$ = 13.6 to 35.2. Interestingly, the aspect ratio ($\delta \approx 3.1$) and the total number of adsorbed catanionic surfactants per P123 micelle (with N_s = 450 ± 70 and N_{ct} = 300 ± 45, at N_p = 11 ± 1) are nearly concomitantly maximized (Fig. 6b) at R = 1.5 and x = 26, with intermediate values of χ_s and χ_{ct}. We notice that despite the continuously enhanced adsorption χ_s with increase of R, the adsorption numbers N_s and especially N_{ct} start decreasing when R increases over 1.5. These features elucidate an intriguing role of the catanionic surfactants in modulating the self-assembly of the surfactant-P123 ternary micelles. With a high adsorption affinity to P123 micelles [33], SDS can facilitate the adsorption of C_{16}TAB to the P123 micelles via co-condensation of the charged ion pairs, leading to optimized prolate micelles for a preferred monolayer self-assembly. However, overly enriched SDS (at high R values) leads to highly charged ternary micelles of high χ_s values (Fig. 6a), which would not favor the subsequent deposition of the also negatively charged silicate source. Consistently, our thermogravimetric analysis (Fig. S-4, SI) indicates that increase of the R value (surfactants) leads to decreased silicate deposition on the P123-surfactant micelles. Altogether, the complementary SANS and SAXS results indicate that shape and composition of the complex micelles of P123-surfactants could be tailored via compound tuning of the ternary mixing ratios of R and x. Below, we show how these structural features of the complex micelles could lead to a best yield of SBA(⊥) synthesis, using time-resolved SAXS and FFR-TEM.

3.2.2. Tracking self-assembly of the silicate micelles

We further traced the self-assembly process of the catanionic-surfactant-coated P123 micelles upon silicate deposition in the optimized sample solution with R = 1.5 and x = 26, using in situ SAXS. As shown in Fig. 7a, the SAXS profile measured before adding silicate source can be decently described (Fig. 7a) by a core–shell prolate model, with 2a = 15.5 nm and 2b = 5.3 nm (cf. Fig. S-5, SI). At t = 7 min with the silicate source added, emergence of three periodic broad peaks indicates formation of lamellar domains (Fig. 7a). From the first peak located at q = 0.064 Å^{-1}, a lamellar spacing of 9.8 nm is extracted. Such size is smaller than the major axis (15.5 nm) but larger than the minor axis (5.3 nm) of the initial prolate micelles upon silicate addition. Most likely, the lamellar spacing results from a lateral packing along the equatorial plane of the prolate micelles. As the silication process evolves, the lamellar peaks shift toward lower-q region with time, revealing a continuous expansion of the lamellar spacing from 9.8 to 12.5 nm (Fig. 7b). These peaks, however, deteriorate gradually and disrupt largely at t ~ 60 min. (Fig. 7a). After another 50 min. of incubation to t = 111 min, a small but relatively sharp peak at q = 0.050 Å^{-1} emerges and enhances in intensity gradually to a prominent primary peak at 0.048 Å^{-1}, which further develops into a 2D hexagonal packing (t = 190 min) with weaker higher-order peaks (cf. Fig. S-6, SI). Moreover, the peak position and width of the primary peak maintain largely constant during its intensity growth, suggesting a nucleation-dominated formation [35] of hexagonally packed domains of a lattice of 12.6 nm and domain sizes of ~350 ± 30 nm (estimated from the peak position and width) [42]. We note that the transition of lamellar to 2D hexagonal

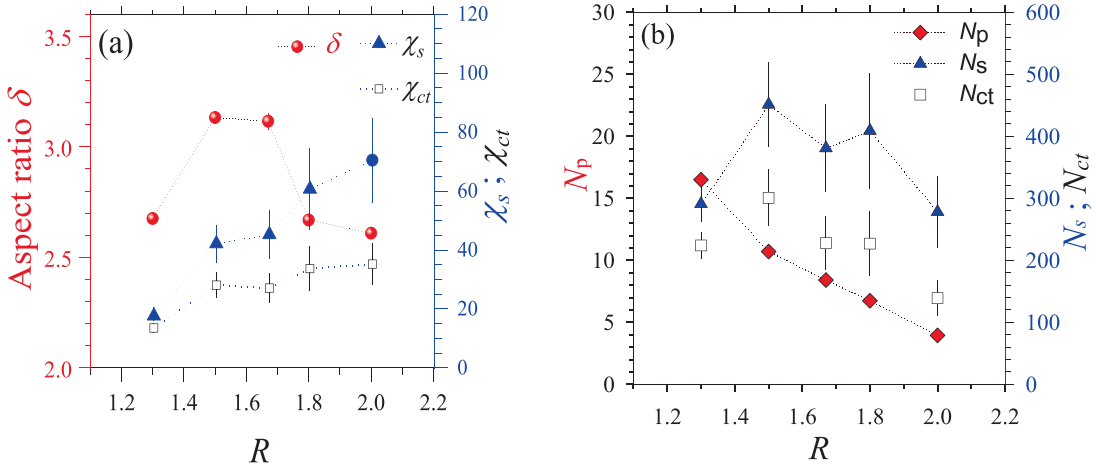

Fig. 6. (a) R-dependent aspect ratio δ and binding ratios $\chi_s = N_s/N_p$ and $\chi_{ct} = N_{ct}/N_p$ of the ternary micelles of P123, SDS, and C_{16}TAB. (b) Corresponding SDS and C_{16}TAB adsorption numbers N_s and N_{ct}, and P123 aggregation number N_p. Note that δ, N_s, and N_{ct} are maximized near R = 1.5.

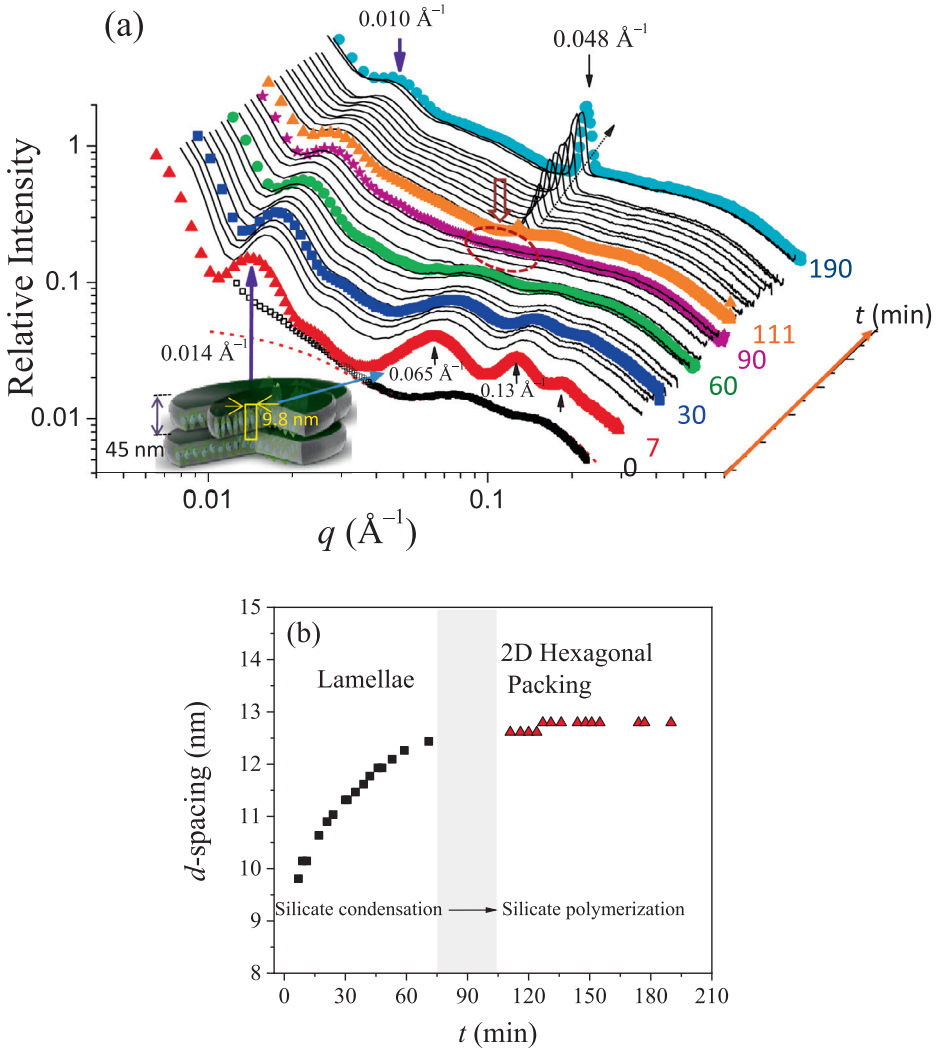

Fig. 7. (a) Time-resolved SAXS profiles measured for an optimized sample solution of P123 and catanionic surfactants (with R = 1.5 and x = 26), before (t = 0) and after addition of silicate source. The higher-q data at t = 0 are fitted (dotted curve) with prolate core–shell micelles. The short arrows mark the three lamellar peaks of the profile at t = 7 min. The low-q peak at 0.014 Å^{-1} corresponds to a vertical stacking order (45 nm d-spacing) of the micellar plates as illustrated by the cartoon. The dotted circle covering t = 60–110 min. marks the transition zone from the lamellar to 2D hexagonal packing. (b) Increase of the in-plane lamellar d-spacing of the micellar plates during the silicate condensation stage along the reaction time t. The shaded zone marks an incubation period prior to the transition to 2D hexagonal packing in the subsequent silicate polymerization stage.

packing could not be observed in those reported SBA syntheses without adding the catanionic surfactants [42–45]. The silica source of sodium silicate used in this study (leading to slower hydrolysis reaction and silicate polymerization in the solution of pH value ~5, compared to tetraethyl or tetramethyl orthosilicate used in previous studies [42–45]), could also contribute to the formation of the intermediate lamellar structure observed. A previous report [42] showed that slower kinetics could lead to formation of intermediate lamellar structure prior to 2D hexagonally ordered silica structure of MCM41 [42]. Fig. 7b further reveals a smooth transition of the final lamellar spacing 12.5 nm to the initial Bragg d-spacing = 12.6 nm of the 2D hexagonal packing, implying that the reorganization of the micelle packing is driven by silica polymerization for tighter packing of the silicate rod micelles, with only marginal size growth.

In the low-q region of the in situ SAXS data (Fig. 7a), a broad hump emerges at q = 0.014 Å^{-1} and evolves to q = 0.01 Å^{-1} over the 190 min reaction time (Fig. 7a). The corresponding Bragg d-spacing increases from 45 nm to 65 nm, prior to the transition of lamellar-to-hexagonal packing of the micelles. Interestingly, this saturated d-spacing (65 nm) is close to the channel length (thickness) of the final silicate micellar plate (~70 nm as revealed by the TEM image shown below), suggesting that orientation alignment of the aggregate plates along the channel direction would result in the Moiré patterns observed previously [17].

Shown in Fig. 8 are the time-resolved FFR-TEM images, parallel to the in situ SAXS. Fig. 8a and b, with and without the relatively small silicate P123-surfactant micelles (~15 nm in size), collectively show the before and after coalescence of the small silicate micelles into the seeded nanoplates within 5 min. The hence enlarged micellar plates exhibit in-plane locally layered domains of the silicate micelles (inset of Fig. 8b). The captured self-assembly behavior strongly supports the proposed silicate transport and silicate deposition respectively with the small surfactant-P123 micelles and their self-assembled nanoplates. Further coalescence growth of the silicate plates was observed after 30 min. of reaction (Fig. 8c). At 120 min, the silicate plates already developed into large sheets, with preliminary 2D hexagonally

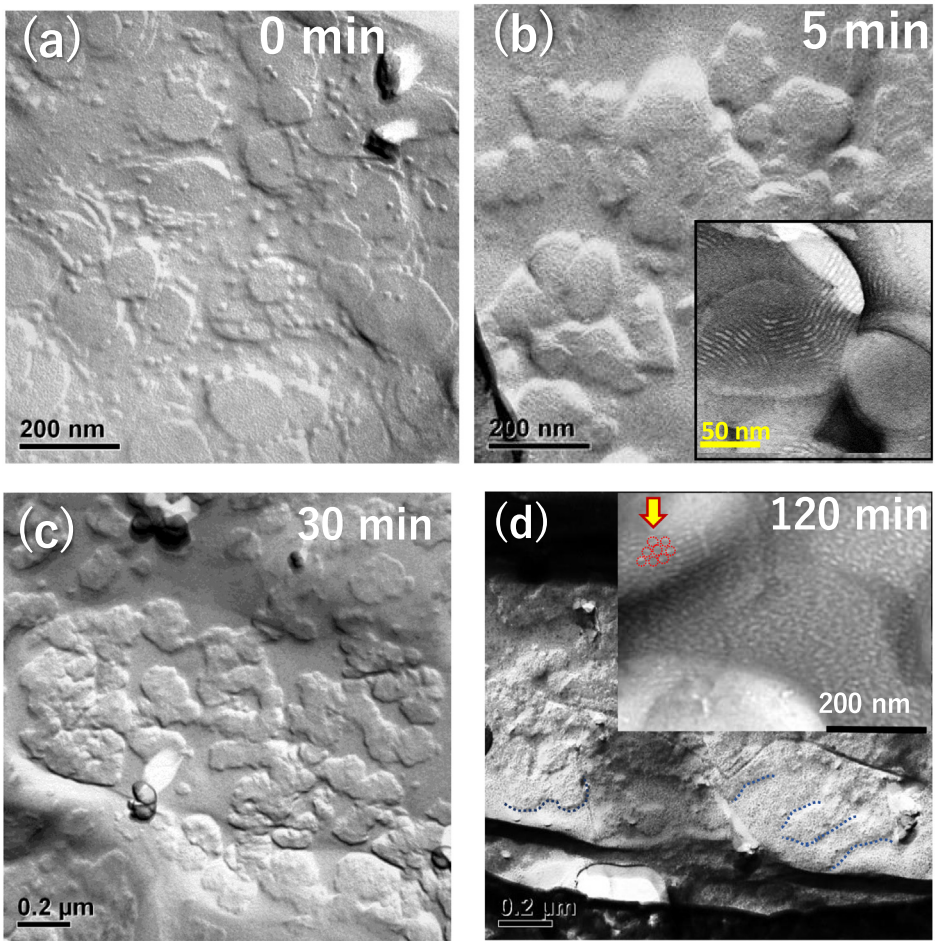

Fig. 8. Time-resolved FFR-TEM images presenting the structural evolution of the silicate micelles of P123 and catanionic surfactants (with R = 1.5 and x = 26) at reaction times (a) t = 0, (b) 5 min., (c), 30 min, and (d) 120 min. The TEM images in the insets of (b) and (d) respectively show in-plane, locally-ordered lamellar domains (bright, rod-like stripes) and 2D hexagonal packing (representatively circled in the inset). The faded domain boundaries are outlined by dotted curves in (d).

packed domains (inset of Fig. 8d). These FFR-TEM snapshots capture the micellar fusion, intermediate structures, and phase transition, which behaviors coincide with those observed in in-situ SAXS.

3.2.3. Orientation alignment of silica channel plates in spin-coated films

Fig. 9a and b show the top and side views of high-resolution TEM images of a silica channel sheet SBA(⊥) prepared under optimized conditions with the molar ratios R = 1.5 and x = 26. These images exhibit 2D hexagonally packed silica channels with open pores, characterized by an average pore size of 9 nm and a channel wall thickness ca. 2 nm [46,47]. The channel length of the through-pore, single-layered, silica sheets is ~70 nm as revealed by the side-view TEM image in the inset of Fig. 9b. Shown in Fig. 9c is a grazing incidence small-angle X-ray scattering (GISAXS) pattern taken for the silicate sheets, spin-coated on silicon substrate from an optimized sample solution. The GISAXS pattern exhibits oriented scattering strips along the vertical direction (q_z), corresponding to a monolayer structure [46]; the corresponding in-plane peak positions (q_r) could be indexed as 2D hexagonal packing for the single-layered silica channels. The characteristic Bragg d-spacing extracted from the (10) reflection peak position is 11.0 nm. The single-layer feature of the spin-coated channel sheets is further characterized with an SEM image in the inset of Fig. 9d with a film thickness ~70 nm, which matches with the channel length shown in the TEM image (inset of Fig. 9b). All these structural features of SBA(⊥) closely associate with those observed in solution, revealing a successful silicate templating via the control of self-assembly behavior of the complex micelles of P123 deposited with charged catanionic surfactants.

3.3. Proposed model and implication

On the basis of the observed structural features of the complex micelles of P123 and the catanionic surfactants, a formation process of SBA(⊥) may now be proposed in Scheme 1. Neat P123 micelles are first condensed with catanionic surfactants of SDS and C_{16}TAB for comparable abundance of small prolate micelles and their self-assembled prototype nanoplates of monolayered micelles, under a controlled environment (x, R, pH value, and reaction temperature). Further silicate condensation on the surfactant-P123 micelles activates the self-assembly of the silicate micelles into monolayered micellar plates of local lamellar packing. Subsequent silica polymerization within the micellar plates initiates an in-plane phase transition of the lamellae to 2D hexagonal packing of the silicate micelles. Via spin-coating, these thin sheets of 2D-ordered silicate rod micelles are aligned further on a solid substrate, then calcined into vertically oriented silica channels with through-pores. The observed open-channel feature implies that rod micelles in the plate aggregate sheets might be largely capped with negatively charged surfactant bilayers, which disfavor silicate deposition; consequently, these surfactant endcaps could be removed relatively easily in calcination for the open-pore silica channel sheet. We also found that the lateral coalescence of the

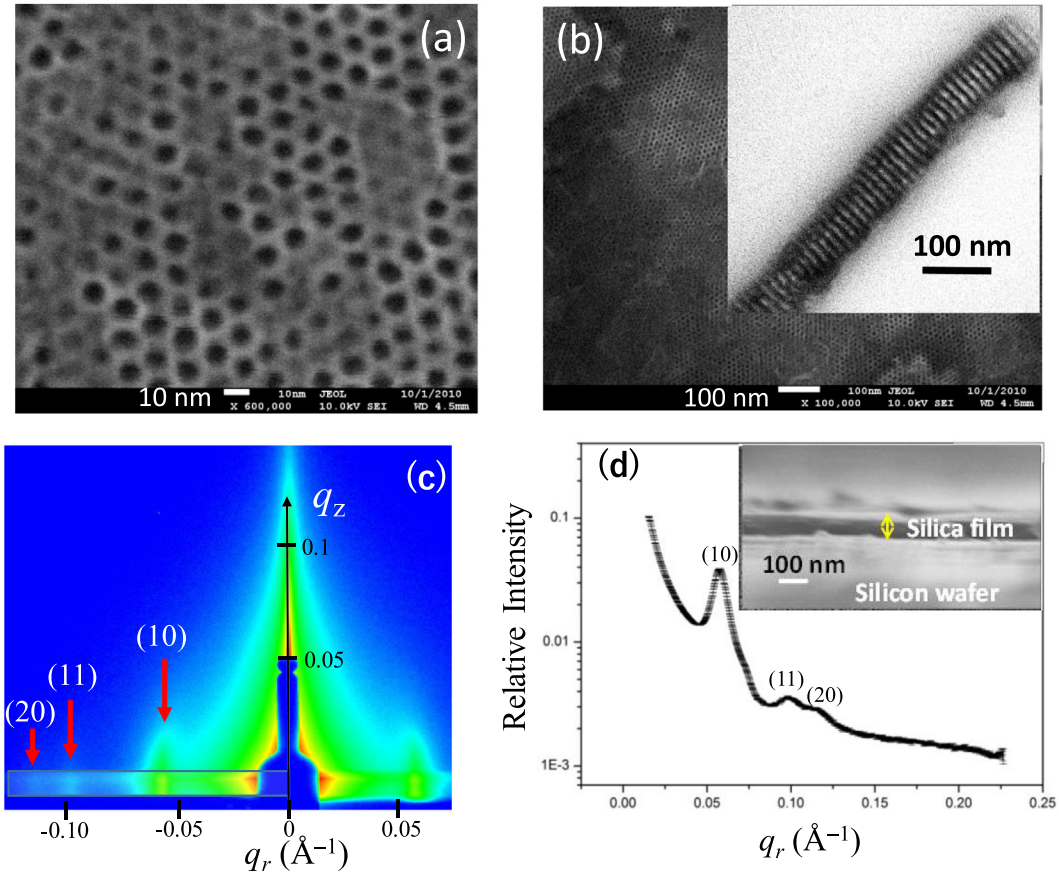

Fig. 9. (a) A TEM top-view image of the silica channel sheet of SBA(⊥) with hexagonally packed open pores (dark zones). (b) A global view of the silica channel sheet in the background, topped with a side-view TEM image showing the features of vertically oriented nanochannels with through-pores (white stripes) and a high channel aspect ratio of ca. 7. (c) Corresponding GISAXS pattern with vertically oriented scattering strips (indicated by arrows), with the in-plane ordered peak positons along q_r indexed with 2D hexagonal packing. (d) Corresponding in-plane GISAXS profile extracted from the 2D pattern along the rectangular area marked in (c); the inset is an SEM image of the spin-coated film.

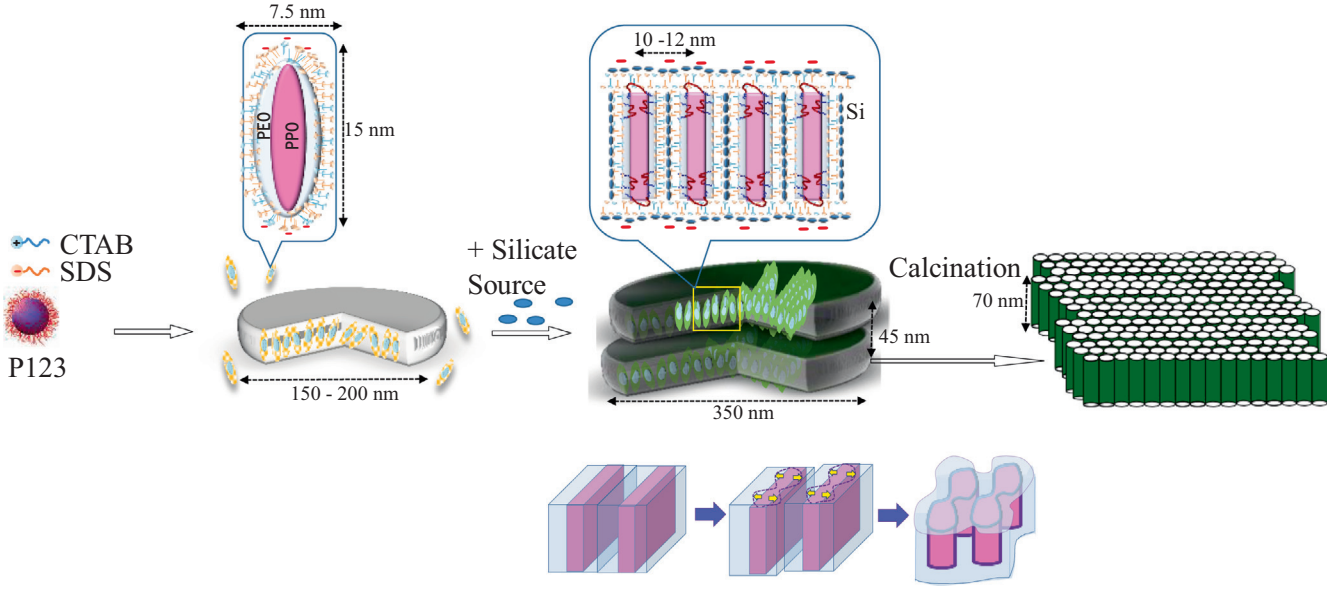

Scheme 1. A proposed process for formation of vertically oriented and organized silica nanochannels. Starting from spherical P123 micelles on the left-hand-side, addition of SDS/C_{16}TAB catanionic surfactants (with significant excess of SDS) leads to negatively charged (– sign) surfactant-P123 core–shell prolate micelles and their self-assembled prototype nanoplates. This is followed by silicate condensation (small blue dots) for micellar self-assembling into large silicate thin sheets. Within which, the silicate micelles form locally in-plane layered packing then transit into elongated micelles of in-plane 2D hexagonal packing (bottom cartoons). Calcination of the silica sheets leads to single-layered, vertically oriented and ordered silica nanochannels with through pores (cartoon to the right).

silicate micellar plates could be further enhanced by elevation of reaction temperatures, resulting in increasingly thinner plates with shorter channel lengths (cf. the SEM images in Fig. S-7, SI); this result also supports that silica condensation and polymerization of the silicate prolate micelles proceed mainly along the lateral direction for favored sheet-like structures.

In diatom frustule morphogenesis, the cell wall silicification process proceeds with templating polyamines and charged proteins that are rich in polar serine and charged lysine residues. The rod-like polyamines serve as silica transportation micelles inside the SDV lumen of diatoms; the charge proteins anchor onto the lipid bilayers of SDV membrane, somehow, regulating the subsequent self-assembly for 2D-membrane-dominated silica patterning [5,12,48,49] into organized silica channel pores beneath the SDV membrane. In our proposed synthesis process of membrane-wall-like silica channels of SBA(⊥), the prolate P123 micelles coated with charged catanionic-surfactant bilayers and their self-assembled prototype nanoplates, to some extent, play analogous roles of the silicate transportation micelles and the silica deposition vesicles in the frustule formation of diatoms.

4. Conclusions

The long speculated formation process of thin silica sheets with perpendicular nanochannels of through pores are elucidated by the structure, composition, and self-assembly behavior of the complex micelles comprising P123 and the catanionic surfactants of SDS and C_{16}TAB. With a combined analysis of SAXS and SANS, the ternary prolate core–shell micelles optimized for synthesis of SBA(⊥) are found to have maximized aspect ratio of ca. 3 and maximized adsorption numbers of 450 and 300 for SDS and C_{16}TAB, and a P123 aggregation number of 11. Charging and shaping play two key parameters in the self-assembly process of the ternary micelles in forming comparable populations of charged prolate core–shell micelles and their prototype nanoplate aggregates, prior to silica deposition. These features, not recognized in previous studies [16,17], are of critical importance in balancing the subsequent silicate transportation and silicate deposition process. Time-resolved observations of SAXS and FFR-TEM have coherently evidenced a lateral fusion of the silicate micelles into the seeded nanoplates, and captured a pivotal phase transition of in-plane lamellarly packed silicate micelles into in-plane 2D hexagonal packing. These intermediate structures elucidate the previously unresolved silicate redistribution process [14,16–17,41–45]. The directional self-assembly modulated by charging and shaping of ternary micelles of catanionic surfactants and copolymers might be extended to multi-stage self-assembly with tunable orientation preference for hierarchical patterning of silica architectures beyond that demonstrated previously [12,13].

Biogenesis of diatom biosilica is a bottom-up process that occurs in large intracellular compartments of silica deposition vesicles of diatoms [50]. Cell biologists and materials scientists alike have been intrigued by the capability of SDVs on producing intricately patterned biosilica structures. Investigating the silica morphogenesis mechanisms has so far been severely limited by the lack of a chemical synthetic system that simulates the SDV behavior in diatoms. In our three-component surfactant system undergoing silica condensation, we have demonstrated a self-assembly of P123/silicate confined in SDV-like bilayer (SDS/CTAB)-shelled nanoplates. The end products of the synthesis are mesoporous silica nanochannel plates with perpendicular channel orientation analogous to that of diatom frustules; a corresponding formation mechanism is proposed on the basis of the large silica deposition nanoplates of SDV-like confinement effects and small silica transport micelles that are like silica transport vesicles [51], revealed from SAXS, SANS, and FFR-TEM. With these analogous features, thus, we have defined a synthetic system of porous silica that mimics the diatom biogenesis in its primitive form. The reported intricate porous silica formation process not only helps in future designs of mesoporous silica thin film materials in a bio-inspired approach but also paves a road towards understanding the biosilica formation of diatoms under soft confinement [52].

Author contributions

The manuscript was written through contributions of all authors. All authors have given approval to the final version of the manuscript.

Declaration of Competing Interest

The authors declare that they have no known competing financial interests or personal relationships that could have appeared to influence the work reported in this paper.

Acknowledgements

CYM thanks Prof. Richard Gordon (University of Manitoba) for enlightening discussions on diatom biology. This work benefited from the use of the SasView application, originally developed under NSF award DMR-0520547. SasView contains code developed with funding from the European Union's Horizon 2020 research and innovation programme under the SINE2020 project, grant agreement No 654000. Funding supports from Ministry of Science and Technology of Taiwan and program of user cultivation of Taiwan neutron facility (under the proposal 2009-2-074-4 of National Synchrotron Radiation Research Center) are acknowledged.

Appendix A. Supplementary data

Supplementary data to this article can be found online at https://doi.org/10.1016/j.jcis.2020.10.114.

References

[1] W. Yang, P.J. Lopez, G. Rosengarten, Analyst 136 (2011) 42–53.
[2] R.R. Naik, S. Singamaneni, Chem. Rev. 117 (2017) 12581–12583.
[3] R. Ragni, S.R. Cicco, D. Vona, G.M. Farinola, Adv. Mater. 30 (2018) e1704289.
[4] Y. Liu, D. Shen, G. Chen, A.A. Elzatahry, M. Pal, H. Palhu, L. Wu, J. Lin, D. Al-Dahyan, W. Li, D. Zhao, Adv. Mater. 29 (2017) 1702274.
[5] B. Tesson, S.J.L. Lerch, M. Hildebrand, Sci. Rep. 7 (2017) 13457.
[6] C.C. Lechner, C.F.W. Becker, Mar. Drugs. 13 (2015) 5297–5333.
[7] F. Noll, M. Sumper, N. Hampp, Nano Lett. 2 (2002) 91–95.
[8] F.M. Fernandes, T. Coradin, C. Aimé, Nanomaterials 4 (2014) 792–812.
[9] B. Delalat, V.C. Sheppard, S. Rasi Ghaemi, S. Rao, C.A. Prestidge, G. McPhee, M.-L. Rogers, J.F. Donoghue, V. Pillay, T.G. Johns, N. Kroger, N.H. Voelcker, Nat. Commum. 6 (2015) 8791.
[10] J.L. Yang, G.S. Lin, C.Y. Mou, K.L. Tung, Chem. Mater. 31 (2019) 1745–1751.
[11] X. Liu, F. Zhang, X. Jing, M. Pan, P. Liu, W. Li, B. Zhu, J. Li, H. Chen, L. Wang, J. Lin, Y. Liu, D. Zhao, H. Yan, C. Fan, Nature 559 (2018) 593–598.
[12] M. Hildebrand, S.J.L. Lerch, Semin. Cell Dev. Biol. 46 (2015) 27–35.
[13] A. Scheffel, N. Poulsen, S. Shian, N. Kröger, Proc. Natl. Acad. Sci. 108 (2011) 3175–3180.
[14] B.C. Chen, H.P. Lin, M.C. Chao, C.Y. Mou, C.Y. Tang, Adv. Mater. 16 (2004) 1657–1661.
[15] S.B. Lioi, X. Wang, M.R. Islam, E.J. Danoff, D.S. English, Phys. Chem. Chem. Phys. 11 (2009) 9315–9325.
[16] Y.Q. Yeh, H.P. Lin, C.Y. Tang, C.Y. Mou, J. Colloid Interf. Sci. 362 (2011) 354–366.
[17] Y.Q. Yeh, C.Y. Tang, C.Y. Mou, APL Mater. 2 (2014) 113303.
[18] S.E. Sujandi, D.S. Park, S.C. Han, M.J. Han, T. Ohsuna, Chem. Commun. 39 (2006) 4131–4133.
[19] X.G. Cui, S.W. Moon, W.C. Zin, Mater. Lett. 60 (2006) 3857–3860.
[20] S.Y. Chen, C.Y. Tang, W.T. Chuang, J.J. Lee, Y.L. Tsai, J.C.C. Chan, C.Y. Lin, Y.C. Liu, S.F. Cheng, Chem. Mater. 20 (2008) 3906–3916.
[21] E.M. Johansson, J.M. Córdoba, M. Odén, M. Micropor, Mesopor. Mater. 133 (2010) 66–74.
[22] R. Huirache-Acuña, R. Nava, C.L. Peza-Ledesma, J. Lara-Romero, G. Alonso-Núñez, B. Pawelec, E.M. Rivera-Muñoz, Materials (Basel) 6 (2013) 4139–4167.

[23] Z. Teng, G. Zheng, Y. Dou, W. Li, C.Y. Mou, X. Zhang, A.M. Asiri, D. Zhao, Angew. Chem. Int. Ed. Engl. 51 (2012) 2173–2177.
[24] L.A. Feigin, D.I. Svergun, Structure Analysis by Small-Angle X-ray and Neutron Scattering, Springer, 1987.
[25] T.L. Lin, S.H. Chen, N.E. Gabriel, M.F. Roberts, J. Am. Chem. Soc. 108 (1986) 3499–3507.
[26] E.Y. Sheu, Phys. Rev. A 45 (1992) 2428–2438.
[27] S. Manet, A. Lecchi, M. Impéror-Clerc, V. Zholobenko, D. Durand, C.L.P. Oliveira, J.S. Pedersen, I. Grillo, F. Meneau, C. Rochas, J. Phys. Chem. B 115 (2011) 11318–11329.
[28] S. Manet, J. Schmitt, M. Impéror-Clerc, V. Zholobenko, D. Durand, C.L.P. Oliveira, J.S. Pedersen, C. Gervais, N. Baccile, F. Babonneau, I. Grillo, F. Meneau, C. Rochas, J. Phys. Chem. B 115 (2011) 11330–11344.
[29] O.T. Mansour, B. Cattoz, R.K. Heenan, S.M. King, P.C. Griffiths, J. Colloid Interf. Sci. 454 (2015) 35–43.
[30] J.B. Hayter, J. Penfold, Colloid Polym. Sci. 261 (1983) 1022–1030.
[31] M. Kotlarchyk, S.-H. Chen, J. Chem. Phys. 79 (1983) 2461–2469.
[32] J.M. Lin, T.L. Lin, U. Jeng, Z.H. Huang, Y.S. Huang, Soft Matter 5 (2009) 3913–3919.
[33] O.T. Mansour, B. Cattoz, M. Beaube, R.K. Heenan, R. Schweins, J. Hurcom, P.C. Griffiths, Polymers 11 (2019) 109.
[34] S. Geng, Y. Wang, L. Wang, T. Kouyama, T. Gotoh, S. Wada, J.Y. Wang, Sci. Rep. 7 (2017) 39202.
[35] A. Mal, S. Bag, S. Ghosh, S.P. Moulik, Colloid Surface A 553 (2018) 633–644.
[36] I.R. Krauss, R. Imperatore, A. De Santis, A. Luchini, L. Paduano, G. D'Errico, J. Colloid Interf. Sci. 501 (2017) 112–122.
[37] P. Andreozzi, S.S. Funari, C. La Mesa, P. Mariani, M.G. Ortore, R. Sinibaldi, F. Spinozzi, J. Phys. Chem. B 114 (2010) 8056–8060.
[38] U. Jeng, C.H. Su, C.J. Su, K.F. Liao, W.T. Chuang, Y.H. Lai, Y.J. Chang, Y.J. Chen, Y.S. Huang, M.T. Lee, K.L. Yu, J.M. Lin, D.G. Liu, C.F. Chang, C.Y. Liu, C.H. Chang, K.S. Liang, J. Appl. Cryst. 43 (2010) 110–121.
[39] A.V. Feoktystov, H. Frielinghaus, Z. Di, S. Jaksch, V. Pipich, M.-S. Appavou, E. Babcock, R. Hanslik, R. Engels, G. Kemmerling, H. Kleines, A. Ioffe, D. Richter, T. Brückel, J. Appl. Cryst. 48 (2015) 61–70.
[40] P.C. Griffiths, A. Paul, R.K. Heenan, J. Penfold, R. Radha, B.L. Bales, J. Phys. Chem. B 108 (2004) 3810–3816.
[41] A. Heins, V.M. Garamus, B. Steffen, H. Stöckmann, K. Schwarz, Food Biophys. 1 (2006) 189–201.
[42] Y.H. Lai, S.W. Cheng, S.W. Chen, J.W. Chang, C.J. Su, A.C. Su, H.S. Sheu, C.Y. Mou, U. Jeng, RSC Adv. 3 (2013) 3270–3283.
[43] A. Sundblom, C.L.P. Oliveira, J.S. Pedersen, A.E.C. Palmqvist, J. Phys. Chem. C 114 (2010) 3483–3492.
[44] J. Schmitt, T. Kjellman, P. Kwasńiewski, F. Meneau, J.S. Pedersen, K.J. Edler, A.R. Rennie, V. Alfredsson, M. Impéror-Clerc, Langmuir 32 (2016) 5162–5172.
[45] M. Impéror-Clerc, I. Grillo, A.Y. Khodakov, D. Durand, V.L. Zholobenkoe, Chem. Commun. (2007) 834–836.
[46] K.C. Kao, C.H. Lin, T.Y. Chen, Y.H. Liu, C.Y. Mou, J. Am. Chem. Soc. 137 (2015) 3779–3782.
[47] C. Ma, L. Han, Z. Jiang, Z. Huang, J. Feng, Y. Yao, S. Che, Chem. Mater. 23 (2011) 3583–3586.
[48] M. Hildebrand, S.J.L. Lerch, R.P. Shrestha, Front. Mar. Sci. 5 (2018) 125.
[49] A. Kotzsch, P. Gröger, D. Pawolski, P.H.H. Bomans, N.A.J.M. Sommerdijk, M. Schlierf, N. Kröger, BMC Biology 15 (2017) 65.
[50] C. Heintze, P. Formanek, D. Pohl, J. Hauptstein, B. Rellinghaus, N. Kröger, BMC Mat. 2 (2020) 11.
[51] V.V. Annenkov, T.N. Basharina, E.N. Danilovtseva, M.A. Grachev, Protoplasma 250 (2013) 1147–1155.
[52] M. Bobeth, A. Dianat, R. Gutierrez, D. Werner, H. Yang, H. Eckert, G. Cuniberti, BMC Mat. 2 (2020) 12.